

Stress-induced patterns in ion-irradiated Silicon: a model based on anisotropic plastic flow

Scott A. Norris

Department of Mathematics

*Southern Methodist University, Dallas, TX 75275**

(Dated: July 23, 2012)

Abstract

We present a model for the effect of stress on thin amorphous films that develop atop ion-irradiated silicon, based on the mechanism of ion-induced anisotropic plastic flow. Using only parameters directly measured or known to high accuracy, the model exhibits remarkably good agreement with the wavelengths of experimentally-observed patterns, and agrees qualitatively with limited data on ripple propagation speed. The predictions of the model are discussed in the context of other mechanisms recently theorized to explain the wavelengths, including extensive comparison with an alternate model of stress.

PACS numbers: 81.16.Rf, 79.20.Rf, 68.35.Ct

arXiv:1207.5754v1 [math-ph] 24 Jul 2012

* snorris@smu.edu

I. INTRODUCTION

Among the many nanoscale patterns that have been observed on ion-irradiated surfaces [1, 2], the discovery of hexagonal arrays of high-aspect ratio dots on Ar^+ -irradiated GaSb [3] has sparked a flurry of experimental and theoretical study into spontaneous pattern formation as a potential route to “bottom-up” fabrication of nanoscale devices. A growing body of evidence increasingly suggests that highly-ordered structures occur only for targets containing more than one material [4–6]. Although early observations of dot formation on pure Silicon [7–9] sparked a series of proposed explanations for the ordered structures [10, 11], none turned out to be viable [12, 13]: ultimately, dots disappeared when impurities and geometric artifacts were carefully removed [14], and reappeared upon their systematic re-introduction [4, 15–17]. As a result, much recent attention has focused on theories of irradiated binary materials [6, 18–23].

Despite these results on the formation of ordered structures, the study of monatomic targets remains important because of commonalities between binary and monatomic systems, and the relative simplicity of the latter. In particular, because it is readily amenable to molecular dynamics simulation, and its near-surface region is amorphous under ion bombardment, noble-gas ion irradiation of silicon has been an important system for comparison between experiment, theory, and simulation of pure materials. This allows rapid development and testing of theories on the basic physical processes of ion irradiation, which occur on two time scales. On timescales of individual ion impacts, spanning $\sim 10^{-9}$ sec and described as the *prompt regime*, there is erosion of some target atoms away from the target [24–26], and redistribution of others to new locations [11, 27]. On much longer timescales associated with kinetic relaxation, spanning around $\sim 10^2$ sec and denoted the *gradual regime*, there is the possibility of surface diffusion [26], stress buildup [28], and viscous flow [29]. The understanding of these basic processes, which remain important in binary materials, continues to evolve in important ways, bringing closer the goal of a theory developed enough to make accurate predictions on irradiation-induced structure formation.

In this paper, we investigate the effect on morphology evolution of stress buildup and relaxation in the thin film of material affected by ion irradiation. We choose a different approach than a recent series of papers on this topic [30–32], which cast the role of stress

in terms of classical fluid dynamics results on gravity-driven flows [33]; the relationship between that model and our own will be discussed in detail in Section IV. Here, instead, we draw analogy with the large literature on ion-induced stress for irradiation at energies in the MeV range, where incoming ions are primarily slowed by electronic stopping [34–39]. There, incoming ions induce an anisotropic deformation in the material, leading to stress buildup. More recently, this effect has also been observed during irradiation in the keV range [40], and the mathematical form of the model has been successfully used to describe a number of phenomena at even lower energies where nuclear stopping is dominant [41, 42]. Based on these results, we here apply the model formally to pattern formation at low energies. We find that our model is able to predict the observed wavelength to remarkable accuracy without the need to estimate any unknown parameter values. We also find it makes predictions on the ripple propagation speed that are consistent with experimental observations.

II. MODEL

We consider the morphological evolution of the top layer of a monatomic target, irradiated by noble gas ions at an incidence angle θ . The ions penetrate a certain average distance into the solid before initiating a collision cascade of atomic displacements. Over many impacts, the accumulated damage induced by these cascades amorphizes a thin film of material atop the target, with a crystalline/amorphous boundary at the bottom the film, and a free boundary at the top of the film. We construct a co-ordinate system in which the (planar) target is perpendicular to the z -axis, with $z = h(x, y)$ tracking the top free boundary, and $z = g(x, y)$ tracking the bottom boundary. We will then consider the effect of stress on the stability of this configuration. In this paper, we will focus exclusively on the effect of stress, and therefore neglect the prompt regime of sputtered atoms [24, 26], or those redistributed to new locations [11, 27, 43].

A. Constitutive Law

Basic Material Properties. It has been established for some time that the incoming ions impart an effective fluidity to the amorphous film that is many orders of magnitude larger than that of bulk amorphous silicon [29]. So any treatment of the film must include viscous

effects. Proposals in past years have suggested the additional consideration of elastic effects [9, 11], and a constitutive law including all such effects is [39]

$$\dot{\mathbf{E}} = \frac{1}{2\eta}\mathbf{T} + \frac{1}{2G}\dot{\mathbf{T}} + \frac{1}{9B}\frac{D}{Dt}(\text{tr}\mathbf{T})\mathbf{I} + \dot{\mathbf{E}}_B \quad (1)$$

Here the first three terms contributing to the linear rate-of-strain tensor

$$\dot{\mathbf{E}} = \frac{1}{2}(\nabla\mathbf{v} + \nabla\mathbf{v}^T) \quad (2)$$

constitute a standard linear model for a Maxwell fluid [44], where \mathbf{T} is the stress tensor, η is the viscosity, G is the shear modulus, and B is the bulk modulus. The final term on the right, $\dot{\mathbf{E}}_B$, is a contribution to this rate of strain due the ion beam. However, it has been argued elsewhere that, in a variety of relevant regimes, the contribution of elasticity should be negligible [13, 42]. Hence, we take the limit of a purely viscous ($G \rightarrow \infty$) and incompressible ($B \rightarrow \infty$) fluid. In the incompressible limit, however, a hydrostatic pressure term must also be included, leading to the simpler constitutive law we will consider for the remainder of this work,

$$\mathbf{T} = -p\mathbf{I} + 2\eta(\dot{\mathbf{E}} - \dot{\mathbf{E}}_B), \quad (3)$$

which is nearly equivalent to a Newtonian fluid, except for the addition of the constant contribution $-2\eta\dot{\mathbf{E}}_B$ to the stress.

Effect of Stress. We now turn to the modeling of stress. Recent work by Castro, Cuerno, and co-workers has appealed to analogy with familiar concepts in fluid dynamics by assuming that the microscopic mechanism stress generation can be coarse-grained into an effective body force [30, 31]. We will discuss that approach in Section IV, but will here take a different approach, attempting to connect more directly with the microscopic process. At that scale, MD simulation has shown that each impact significantly redistributes the target silicon atoms to new locations [43, 45, 46], gradually increasing the magnitude of a compressive stress to a saturated state [47], which is also observed experimentally [48]. Each impact thus induces a direct deformation of the material, suggesting that the effect of the beam be incorporated directly into the constitutive relationship between stress and strain, in a way that depends linearly on the total fluence.

A model with exactly these properties has already been developed to describe anisotropic plastic flow during high-energy ion irradiation in the regime of electronic stopping, where

rapid thermal cycling due to ion impacts leads to a stress-free strain rate of the form [34, 35, 38, 39]

$$\dot{\mathbf{E}}_B = fA\mathbf{D}(\theta). \quad (4)$$

Here, f is the ion flux, A is a measure of the magnitude of strain induced per ion, and \mathbf{D} describes the (anisotropic and angle-dependent) shape of that strain. The *mechanism* behind Eqn.(4) is of course not directly applicable in the nuclear stopping regime. However, the *phenomenon* anisotropic plastic flow has been observed even in the nuclear stopping regime [40], and the *mathematical form* of the governing equations has been applied successfully to describe various phenomena at low energies [41, 42]. In this spirit, we have argued elsewhere [13] that, for $\theta = 0$, simple symmetry arguments lead almost immediately to the form

$$\mathbf{D}(0) = \begin{bmatrix} 1 & 0 & 0 \\ 0 & 1 & 0 \\ 0 & 0 & -2 \end{bmatrix} \quad (5)$$

regardless of the underlying mechanism. From here, it is natural to add angle-dependence via the matrix

$$\mathbf{R}(\theta) = \begin{bmatrix} \cos \theta & 0 & -\sin(\theta) \\ 0 & 1 & 0 \\ \sin(\theta) & 0 & \cos(\theta) \end{bmatrix}, \quad (6)$$

describing rotation about the y -axis, which leads to

$$\mathbf{D}(\theta) = \mathbf{R}(-\theta)\mathbf{D}(0)\mathbf{R}(\theta) = \begin{bmatrix} \frac{3}{2}\cos(2\theta) - \frac{1}{2} & 0 & \frac{3}{2}\sin(2\theta) \\ 0 & 1 & 0 \\ \frac{3}{2}\sin(2\theta) & 0 & -\frac{3}{2}\cos(2\theta) - \frac{1}{2} \end{bmatrix}. \quad (7)$$

Combining (3), (4), we obtain the final form of the constitutive relation,

$$\mathbf{T} = -p\mathbf{I} + 2\eta\left(\dot{\mathbf{E}} - fA\mathbf{D}\right),$$

with $\mathbf{D}(\theta)$ given by Eqn.(7).

B. Governing Equations

The governing equations are obtained following standard continuum analysis in the limit of a highly viscous film. In the bulk, conservation of mass in the incompressible limit gives

$$\nabla \cdot \mathbf{v} = 0, \quad (8)$$

the incompressibility condition on the velocity field \mathbf{v} . In addition, conservation of momentum takes the form

$$\rho \left(\frac{\partial \mathbf{v}}{\partial t} + \mathbf{v} \cdot \nabla \mathbf{v} \right) = \nabla \cdot \mathbf{T} + \mathbf{f}, \quad (9)$$

where the left hand side contains the density ρ and the material acceleration, and the right hand side lists forces $\nabla \cdot \mathbf{T}$ due to internal stresses, and \mathbf{f} due to long-range body forces. From here, because of the high viscosity of the ion-irradiated film, accelerations in the left-hand side are small and can be neglected, and we do not consider the effect of any body forces. Hence, we arrive at Stokes equations:

$$\nabla \cdot \mathbf{T} = -\nabla p + \eta \nabla^2 \mathbf{v} = 0. \quad (10)$$

It remains to apply boundary conditions. At the amorphous/crystalline boundary $z = g(x, y)$ we have the combined “no-penetration” and “no-slip” conditions for a viscous fluid;

$$\mathbf{v} = \mathbf{0}. \quad (11)$$

Meanwhile, allowing for the effect of surface tension on a viscous fluid, the stress balance at the free boundary $z = h(x, y)$ can be written

$$\mathbf{T} \cdot \mathbf{n} = -\gamma \kappa \mathbf{n} \quad (12)$$

while the kinematic condition relating bulk velocity \mathbf{v} to the normal surface velocity at the interface, v_I , is

$$v_I = \mathbf{v} \cdot \mathbf{n} \quad (13)$$

We see that the effect of the beam, through the angle-dependent tensor $\mathbf{D}(\theta)$, appears mathematically only at the free boundary in Equation (12), where it alters the conditions necessary for stress balance.

III. ANALYSIS

A. Steady Solution

We first look for a steady state ($\partial/\partial t \rightarrow 0$) consisting of a flat, uniform film occupying the space between $z = g_0$ and $z = h_0$, with pressure p_0 and velocity \mathbf{v}_0 . For convenience we choose $g_0 = 0$. Symmetry considerations greatly simplify the calculations – the assumption of uniformity implies translational symmetry in x and y , which limits the steady pressure and velocity field to be functions of z at most: $p_0(z)$ and $\mathbf{v}_0(z)$. Furthermore, although off-normal ion incidence from the negative x -direction may break reflection symmetry in x , we enforce reflection symmetry in y , which prohibits a velocity component in the y -direction. These considerations immediately limit the form of the steady velocity field \mathbf{v}_0 to

$$\mathbf{v}_0(z) = (u_0(z), 0, w_0(z))^T. \quad (14)$$

Comparing Eqn. (14) to the incompressibility condition (8) and the no-penetration condition (11), we first see that

$$w_0(z) = 0. \quad (15)$$

Next, the z -component of the Stokes equations (10) show the steady pressure to be a constant

$$p_0(z) = a, \quad (16)$$

while the x -component of (10) restricts $u_0(z)$ to at most the linear form

$$u_0(z) = b + cz. \quad (17)$$

Finally, application of the remaining boundary conditions gives us a , b , and c . The no-slip condition (11), applied at $z = g_0 = 0$, requires $b = 0$, while the stress balance condition (12), applied at $z = h_0$, yields $a = \eta f A [3 \cos(2\theta) + 1]$ and $c = 3fA \sin(2\theta)$. In summary, the steady solution is thus

$$\begin{aligned} p_0 &= \eta f A [3 \cos(2\theta) + 1] \\ \mathbf{v}_0 &= (3fA \sin(2\theta) z, 0, 0)^T \\ \mathbf{T}_0 &= -6\eta f A \begin{bmatrix} \cos(2\theta) & 0 & 0 \\ 0 & \cos^2(\theta) & 0 \\ 0 & 0 & 0 \end{bmatrix}, \end{aligned} \quad (18)$$

consisting of a uniform pressure and downbeam shear that both depend on the irradiation angle-of-incidence θ . The pressure is maximum at $\theta = 0^\circ$ and monotonically decreases at higher angles, whereas the shear flow is maximal at $\theta = 45^\circ$ and decays to zero for $\theta = \{0^\circ, 90^\circ\}$. We note in particular the form of the steady stress when $\theta = 0$; a symmetric, biaxial compressive stress with no vertical component.

B. Linear Stability

We now perform a linear stability analysis – e.g., we consider the evolution of the system when the top boundary is subjected to an infinitesimal, sinusoidal perturbation in the x - and y - directions. This leads to solutions that can be expressed in terms of *normal modes* having the form

$$\begin{bmatrix} g \\ h \\ p \\ \mathbf{v} \end{bmatrix} = \begin{bmatrix} 0 \\ h_0 \\ p_0 \\ \mathbf{v}_0(z) \end{bmatrix} + \varepsilon \begin{bmatrix} g_1 \\ h_1 \\ p_1(z) \\ \mathbf{v}_1(z) \end{bmatrix} e^{i(k_1x+k_2y)+\sigma t}. \quad (19)$$

Here we do not assume that the bottom boundary remains flat. Instead, as the top boundary changes shape, the zone of material affected by collision cascades changes with it. As a simplest approximation to this behavior, based on the observed weak dependency of film thickness on angle [49], we choose

$$g_1 = h_1$$

indicating that the bottom boundary is simply a vertical translation of the top boundary, as depicted in Figure III C. With this definition, the forms (19) are then inserted into the governing equations (10)-(13), and terms are kept only to leading order in the vanishingly-small parameter ε . Solution proceeds in three steps, as shown in the Appendix. First, the linearized version of the incompressibility condition (8) and Stokes equations (10) are solved to give a general solution for the pressure and velocity fields in the bulk. Second, the linearized boundary conditions (11) and (12) are applied to determine the resulting integration constants. Last, having uniquely determined the pressure and velocity fields, the application of the kinematic condition (13) leads directly to the *dispersion relation* $\sigma(k_1, k_2)$ governing the evolution of each mode. We find

$$\begin{aligned}
\sigma(k_1, k_2) = & -6fA \frac{\cos(2\theta)(h_0k_1)^2 + \cos^2(\theta)(h_0k_2)^2}{1 + 2Q^2 + \cosh(2Q)} - 3fA \sin(2\theta) i(h_0k_1) \\
& - 3fA \sin(2\theta) i(h_0k_1) \left\{ \frac{2 \cosh(Q) [Q^2 + \sinh^2(Q)]}{1 + 2Q^2 + \cosh(2Q)} - \cosh(Q) \right\}. \quad (20) \\
& - \frac{\gamma}{2\eta h_0} \frac{Q(\sinh(2Q) - 2Q)}{1 + 2Q^2 + \cosh(2Q)}
\end{aligned}$$

where the dimensionless wavevector $Q = h_0 \sqrt{k_1^2 + k_2^2}$. Here the first line corresponds to the effect of anisotropic plastic flow operating on the bulk film, the second line corresponds to the effect (under said flow) of the non-planar bottom boundary $g_1(x, y) = h_1(x, y)$, and the third line corresponds to the well-studied (isotropic) effect of surface leveling under surface tension (see Ref. [50]).

A commonly-employed simplification of Eqn.(20) occurs in the long-wavelength limit $Q \ll 1$ of Eqn.(20), in which wavelength is much longer than the film depth. In this limit the leading-order contributions of each line in Eqn.(20) reduce to

$$\begin{aligned}
\sigma \approx & -3fA [\cos(2\theta)(k_1h_0)^2 + \cos^2(\theta)(k_2h_0)^2] \\
& - \frac{9}{2}fA \sin(2\theta) i(k_1h_0) Q^2 \\
& - \frac{\gamma}{3\eta h_0} Q^4
\end{aligned} \quad (21)$$

This approximation is useful by nature of being much simpler than Eqn.(20). However, despite being commonly employed, this assumption is less commonly verified against experimental data. For instance, in the experiments of Madi [9, 51], widely used as a point of comparison with theory, the film thickness $h_0 \approx 3$ nm, while wavenumbers are as large as $k \approx 2\pi/(20 \text{ nm})$, giving $Q \approx 1$. Hence, while we include Eqn.(21) for reference and use in qualitative discussion, numerical predictions will be based on the full Eqn.(20).

C. Discussion of Results

Stability. The real terms

$$r(k) = \text{Re}[\sigma(k)]$$

from Eqn.(21) describe the *growth rate* of perturbations to the flat steady state in terms of their wavenumber k . The value of k that maximizes $r(k)$ - denoted k^* - is called the *most*

unstable mode; if $\sigma(k^*) < 0$, then all modes decay and the steady solution is *stable*, whereas if $\sigma(k^*) > 0$, then at least some modes near k^* grow, and the steady solution is unstable. From the full dispersion relation (20), we see that a positive band of unstable wavenumbers exists if $\theta > 45^\circ$. In the longwave approximation (21), the most unstable wavelength is given by

$$\lambda^* \approx 2\pi \sqrt{\frac{2\gamma h}{9fA\eta \cos(2\theta)}} \approx 2\pi \sqrt{\frac{4\gamma h}{3|\mathbf{T}_0(0)| \cos(2\theta)}} \quad (22)$$

where the denominator inside the radical is identified as a multiple of the steady in-plane stress at normal incidence, as given by Eqn.(18). This is convenient, because it allows replacing the estimation of the infrequently-measured ion-enhanced viscosity η , and the stress-per-ion parameter A , with an experimental observation of the steady stress at normal incidence. Hence, we can compare existing measurements of the steady stress and the wavelength for the same material under identical irradiation conditions. It has already been shown by Madi that at 250 eV, $h \approx 3$ nm and $|\mathbf{T}_0(0)| \approx 1.5$ GPa [48], while in the same chamber at the same energy, wavelengths given by Figure III C were observed [9, 14, 51]. With the additional value $\gamma = 1.36$ J/m [52, 53], we can compare the stress measurements to the observed wavelengths. We find that the full dispersion relation predicts a remarkably good fit to the data. Unsurprisingly given the size of Q , the longwave approximation does not do nearly as well.

Ripple Velocity. The imaginary terms

$$\omega(k) = -\text{Im}[\sigma(k)]$$

from Eqn.(21) (note the conventional minus sign) describe the *propagation rate* of perturbations to the flat steady state because, from the original linear ansatz,

$$\exp(\sigma t + ikx) = \exp\left(rt + ik\left(x - \frac{\omega}{k}t\right)\right). \quad (23)$$

Equation (23) reveals that, in a stationary “lab” frame of reference, individual ripples of wavelength k propagate with a speed

$$V_{\text{phase}} = \frac{\omega(k)}{k}$$

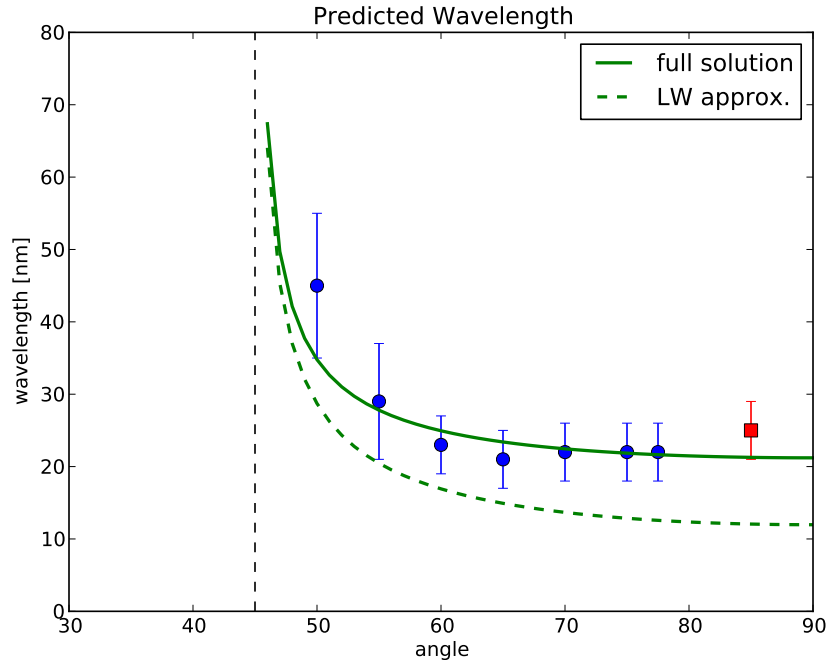


Figure 1. (color online) Wavelength as predicted by numerically maximizing the full dispersion relation (20) over Q (solid line), and under the longwave approximation (21) (dashed line). Given the fixed parameter values indicated in the text, the full dispersion relation predicts the observed wavelengths of parallel-mode ripples (circles) to surprising accuracy, although it does not predict the rotation of the ripples to perpendicular-mode (square) at high angles. Following the discussion the text, we observe that the wavelengths predicted by the longwave approximation differ significantly from those predicted by the full dispersion relation.

usually called the *phase velocity*. Comparison with (21) reveals that, for our problem,

$$V_{\text{phase}} = 3fAh_0 \sin(2\theta) \left\{ \frac{2 \cosh(Q) [Q^2 + \sinh^2(Q)]}{1 + 2Q^2 + \cosh(2Q)} - \cosh(Q) \right\} \approx \frac{9}{2} fAh_0 \sin(2\theta) Q^2. \quad (24)$$

Although limited experimental data on ripple velocities is available, what reports exist indicate that - contrary to early seminal theory concerned only with erosion [26] - ripples always propagate in the direction of the ion beam [54, 55]. Both our longwave result (24), and also the velocity resulting from the full dispersion relation (20), are uniformly positive for all values of θ or Q , consistent with these observations.

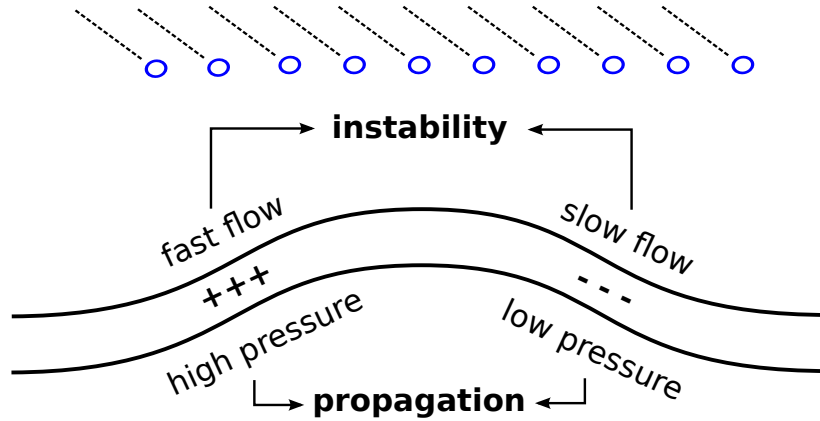


Figure 2. Schematic of the system, illustrating the intuitive understanding of ripple growth and propagation.

Intuitive Explanation of Ripple Growth and Propagation. Both the instability and translation mechanisms can be understood intuitively in terms of simple differences in the steady shear flow and pressure across a ripple. The instability occurs when the net shear flow on the uphill side exceeds the net flow on the downhill side. We recall that the flow rate has a maximum when the local angle of incidence is 45° , and decreases monotonically for as the local angle continues to increase. So, when $\theta > 45^\circ$, then uphill slopes (with angle closer to 45°) have greater flow than downhill slopes (with higher angle), leading to mass accumulation at the top of the ripple. Similarly, ripple translation occurs because the steady pressure is a monotonically decreasing function of incidence angle. Hence, for any angle, the pressure in the uphill side exceeds that in the downhill side, leading to flow from uphill to downhill slopes, as indicated in Figure III C. We note that this ripple propagation mechanism is almost entirely driven by the nonplanar nature of the bottom boundary; if the bottom boundary were instead flat, the only contribution to the phase velocity would come from the last term of the first line of (20), which indicates simple translation along with the shearing film. However, when the translated bottom boundary is included, it exactly cancels this simple shear in the long-wavelength limit, and the resulting ripple propagation is entirely due to differences in pressure across a ripple.

Relationship to thermal stress models. The contribution (24) to the ripple velocity, and indeed several aspects of the analysis used to attain it, bears a notable resemblance to the work of Alkemade on ripple propulsion [54]. There, the author proposes a mechanism of ripple propagation that also is caused by variations in the stress, but in which the stress itself is caused by thermal expansion. Briefly, larger relative depth of the uphill slopes causes higher sustained temperatures there, leading to greater thermal expansion and thus greater thermal stress. The problem is that at the scale of the ripple size ($\sim 20 - 50$ nm), thermal diffusion is so rapid that no meaningful temperature differential can be sustained. Our model can be thought of as an alternative to this mechanism, where the source of stress is purely mechanical, requiring no thermal gradients, and variation appears naturally as a result of the different slopes inherent to a ripple structure.

IV. RELATIONSHIP TO EFFECTIVE BODY FORCE MODELS

We will now attempt to give a comprehensive comparison of our theory with another recent model of stress that appeals to analogies with fluid dynamics [30–32] by rendering the effect of stress as an “effective body force” (EBF) which acts throughout the amorphous film. The bulk of the the EBF model is developed in Ref.[31]. There, the effect of the beam is posited to lie within the constitutive relation via

$$T_{ij} = -p\delta_{ij} + \mu (\partial_i v_j + \partial_j v_i) + T_{ij}^s, \quad (25)$$

which is effectively identical to our Eqn.(1), and similar to work dating at least to Ref.[39]. However, the authors never explicitly define the tensor T_{ij}^s describing the effect of the beam, instead proposing only that its divergence takes the form

$$\nabla \cdot \mathbf{T}^s = \mathbf{b} = \mathbf{f}_E \Psi(\theta - \gamma) \quad (26)$$

where the authors “define $\mathbf{b} = \nabla \cdot \mathbf{T}^s$ as a body force acting in the bulk of the fluid layer.” Although the incoming ions undoubtedly exert a force on the film as they are slowed down by the film, that force can be shown to be vanishingly small [49], and Eqn.(26) is not suggested to represent any actual physical force. Instead, \mathbf{f}_E is proposed to contain “the coarse-grained information about the effect of the residual stress created in the target ... [with] dimensions of a gradient of stress,” and $\Psi(\theta - \gamma)$ to encode dependence upon the local angle of incidence

$\theta - \gamma$. This is an interesting effort to encompass the many complexities of the nonlocal ion irradiation process within a familiar, intuitive form, and seems to achieve good agreement with experiment. It therefore demands reasons for the proposal of an alternative model.

A. Differences with EBF: Fundamental Model

We here present three concerns with the EBF model that are avoided by the present approach.

Surface-Dependent Body Force. The first, primary concern with the EBF model given by Eqn.(26) is its highly unusual suggestion that a “body force” could exist that acts throughout the film, but which contains an explicit dependence on the configuration of some nearby patch of surface. Traditionally, true body forces that can act directly on bulk elements - also known more descriptively as “long-range forces” - are completely independent of nearby surfaces (since the latter are presumably much nearer than the source of the long-range force). Any effects due to surfaces are instead rigorously segregated into boundary conditions, to ensure that the transmission of surface physics into the bulk is mediated by the constitutive properties of the material itself. A formulation like (26) blurs this traditional distinction, suggesting the existence of a mechanism which depends on the surface, but can nevertheless directly inform buried bulk parcels without any consideration of the material in between.

Functional Form of Ψ . A second concern is that, to obtain a good fit with experimental data, the EBF model assumes that the function Ψ take the form $\Psi = \cos(\theta - \gamma)$; i.e., that the body force is proportional to the flux density at the surface. This would be perfectly reasonable if the force \mathbf{b} acted only at the surface - i.e., if it were a surface traction - because it reflects the geometric dilution of the beam as the orientation of the surface varies relative to the beam orientation. However, the force \mathbf{b} is instead proposed to act as a long-range force throughout the bulk of the film, and as just discussed, true long-range forces are typically approximately constant in any given location. Hence, the correct form for the angle dependence of Ψ is much less obvious than it first appears, and the plausibility of the assumption $\Psi = \cos(\theta - \gamma)$, upon which good agreement with experiment rests, becomes less certain.

Location of Stress. A final, minor concern is the inclusion of the undefined tensor \mathbf{T}^s into the stress \mathbf{T} . True body forces are traditionally not included within the stress tensor itself, but rather constitute a separate item in the equations of conservation of momentum (9). The distinction is subtle: the resulting equations for the *velocity field* are the same in either case, but once velocities have been calculated, the resulting *stress field* (3) depends qualitatively on the location of the effects of the beam. So within the EBF model, if the effect of the beam is genuinely supposed to appear within Eqn.(25), then \mathbf{T}^s must be rigorously defined because, as a part of the full stress \mathbf{T} , it must play a role in the balance of forces at the free interface $z = h(x, y)$. However, if the effect of the beam is truly to be treated as a body force (as seems to be the intent), then it should not appear in Eqn.(25).

Comparison with the present model. In contrast to these dilemmas inherent in the EBF model as currently proposed, the model presented here maintains the traditional location and form of terms, and makes fewer assumptions to achieve good agreement with experiment. In particular, the ion beam acts within the bulk constitutive law (1) as a true tensor describing stress-free anisotropic plastic flow. Acting as it does throughout the entire body of the film, it is completely independent of the surface configuration, as a traditional long-range mechanism should be. And, as a true tensor, it is fully defined via Eqn.(7) and included in the force balance (12) at the free boundary. Finally, by starting at a level closer to the microscopic process, our model based on the mechanism of anisotropic plastic flow requires fewer, and weaker, assumptions. In particular, the correct angular dependence of the wavelength on the irradiation angle arises very naturally merely from the simple rotation of the strain tensor with the beam.

B. Differences with EBF: Theoretical Predictions

In addition to fundamental differences at the level of modeling, the present theory also differs from the EBF theory in terms of experimental predictions.

Steady State. The two models for stress produce different steady states. We first observe that, in contrast to the constant pressure and linear flow profile found here, Ref.[31] reports a depth-dependent pressure and quadratic flow profile. This results in qualitatively different scalings for the net flow through the film: d^2 vs. d^3 , which could be significant given the

small size of d . Next, combining Eqs.(4),(15-17) from Ref.[31], one can show that the EBF model results in a steady stress throughout the film of

$$\mathbf{T}_{EBF} = f_E \Psi(\theta) z \begin{bmatrix} \cos(\theta) & -\sin(\theta) \\ -\sin(\theta) & \cos(\theta) \end{bmatrix} + \mathbf{T}^S, \quad (27)$$

where the second component \mathbf{T}^S remains undefined within the EBF theory, and should potentially be omitted, as discussed above. Focusing on first part associated with viscous stress, we observe two differences with our Eqn.(18). First, the magnitude of the viscous stress increases as the distance from the free surface increases, reaching a maximum at the crystalline/amorphous interface $z = -d$. However, considering that this stress is due to incoming ions which are slowed by the film, one would expect the effect of the beam to at most remain constant with film depth (as assumed here in Eqn.(18)), or, perhaps more realistically, to decay with film depth. Second, Eqn.(27) has a different shape than our Eqn.(18), with different angular dependence and principal stress directions, which may be detectable using wafer curvature measurements. In particular, when dotted with the upward-pointing unit vector $\hat{\mathbf{k}}$, Eqn.(27) indicates the presence of stress along the vertical direction; however, unless a body force is truly present, the flat free boundary should allow all stress in the vertical direction to relax to zero (as seen here in Eqn.(18)).

Wavelengths. A noteworthy success of the EBF theory is the apparently remarkable agreement of its predictions on wavelength with experimental data; our Figure (III C) is nearly identical to Figure 3 of Ref.[31]. However, it turns out that the remarkable agreement with experiment depicted in that figure were based on incorrect data. Taking the geometric mean of MD estimates of 1.62 GPa [56], and preliminary experimental data of 200 MPa [51], the authors estimate the magnitude of the stress to be 569 MPa. This value then leads to an estimate of $|\mathbf{f}_E| = 0.424 \text{ kg}/(\text{nm s})^2$, producing the good fit with data. However, the lower, experimental value of the stress was later found to be in error, and a more correct value for Silicon irradiated by Argon at 250 eV has more recently been revised to 1.4 GPa [48]. Although the precise means of calculating $|\mathbf{f}_E|$ are not specified in Ref.[31], if we assume that $|\mathbf{f}_E| \propto |\mathbf{T}_0|$ we may estimate a value associated with the revised stress of $|\mathbf{f}_E| \approx 0.424 \times 1400 \div 569 = 1.04 \text{ kg}/(\text{nm s})^2$, which does not fit the data on wavelengths as well. Put another way, the EBF model seems to over-estimate the effect of stress on growth rate by a factor of about 2-3 relative to the current theory, which provides better agreement

with experiment when correct values of the steady stress are used.

Ripple Velocities. The theory of solid flow developed around the EBF model in Ref.[31] predicts a ripple velocity of the form

$$V_{\text{ripple}} = \frac{d^2 f_E \sin(2\theta)}{2\eta} \left(1 - \frac{3}{8} Q^2 \right) \quad (28)$$

(although the derivation appears to contain a few minor errors, such as the use of the group velocity $\frac{d\omega}{dk}$ instead of the phase velocity $\frac{\omega}{k}$). At first glance, Eqn.(28) appears to have the same $\sin(2\theta)$ angle dependence as our result 24; however, it also bears a few important differences. First, within the parenthesis, Eqn.(28) contains a constant term, and because it is typically assumed that $Q \ll 1$ (though see above), this term should be expected to dominate the ripple velocity for large wavelengths. In contrast, our Eqn.(24) contains no constant term which, because the critical value of Q itself depends on θ , should produce a different functional form of the ripple velocity in terms of the angle. This difference should be especially noticeable near the bifurcation at 45° , where wavelengths become large: our model predicts stationary ripples as $Q \rightarrow 0$, whereas the EBF model predicts moving ripples. Second, Eqn.(28) depends on the ion-enhanced viscosity of the material, but only weakly or not at all on the flux (see Ref.[32] for a discussion of parameter dependencies of f_E). In contrast, our Eqn.(24) does not depend on the viscosity, and depends linearly on the flux, consistent with the hypothesis that each impact induces a fixed amount of anisotropic deformation in the material. These differences should be testable experimentally with measurements of ripple velocity as functions of various experimental parameters.

V. OPEN QUESTIONS

Ripple Rotation. One of the fundamental successes of the original Bradley-Harper theory of erosion was its ability to predict the oft-observed 90-degree rotation of ripples at high angles of incidence [26]. Despite recent studies suggesting that this erosive effect is in fact overwhelmed at most angles by the effect of redistributed atoms [43, 57], no alternative to Bradley-Harper has been able to definitively predict ripple rotation at high angles, and our theory is no exception. It is likely that either erosive effects are still somehow dominant at grazing angle, or that some other effect particular to grazing incidence induces the ripple rotation. (We point out that Johnson et al. recently predicted such a rotation based

on molecular dynamics measurements [58]. However, that prediction rests upon apparent measurements of a *negative* lateral momentum transfer at grazing angles; we have instead observed lateral momentum transfer to be positive at all angles [43]. Comparative study of the methods used to obtain and filter these data would be highly desirable.)

Relationship to Mass Redistribution. A notable observation absent from the discussion surrounding the EBF model is the observation that stress is actually the *second* distinct physical mechanism shown to produce reasonably good agreement with experimentally-observed ripple wavelengths. It has been shown previously that the leading order treatment of 'redistributed' target atoms - those displaced from their original location but not sputtered - produces second derivatives in the dispersion relation (21) of exactly the same form as those reported here [11, 27], and molecular dynamics simulations suggest that these terms are of just the right size to produce reasonably accurate predictions of the observed ripple wavelengths [43]. Because each effect, alone, seems able to predict the correct wavelengths, the combination of both effects would be expected to be wrong.

One possible resolution to this dilemma appeals to the fact that stress, ultimately, is generated by target atom displacements. Hence, morphology evolution due to both target atom redistribution and stress are ultimately driven solely by single ion impacts, just on different timescales. So although they are properly distinct within a timescale-separated framework, one could imagine the possibility of a generalized multi-scale framework which incorporates both the displacements and stresses induced by single ion impacts, as measured by molecular dynamics. In the process of analyzing the contribution to stress (see, e.g., Refs.[47, 56, 59]), the tensor \mathbf{D} is something that could potentially be measured as a function of angle, whereas the effective body force, until it is connected directly with a microscopic mechanism, will likely be more difficult to obtain.

A second possible explanation appeals to uncertainty surrounding the exact value of the ion-enhanced viscosity η , which has only been estimated using molecular dynamics. Whereas the wavelength predictions in Ref.[43] due to mass redistribution relied directly on η , within the present approach it was possible to avoid estimating η by instead measuring the steady stress $|\mathbf{T}_0|$, which can be directly observed experimentally. Hence, while the accuracy of the redistribution model is vulnerable to changes in estimates of η , the accuracy of the anisotropic plastic flow model is not. For this reason, the latter currently appears to this

author to be the more robust. So despite its technical problems, the authors of the EBF model may ultimately be proved correct in their hypothesis that “Solid flow drives surface nano-patterning by ion-beam irradiation” [32].

VI. CONCLUSIONS

In the pursuit of better understanding the role of stress in ion-irradiated films, we have analyzed a model of stress based on the mechanism of anisotropic plastic flow. This approach represents an alternative to a recent “effective body force” (EBF) model of stress based loosely on traditional fluid mechanics results. Based on distinct microscopic mechanism, the model avoids several technical problems in the EBF approach, and achieves remarkable experimental agreement on ripple wavelengths using more accurate experimental parameters and fewer underlying assumptions. In addition, it makes more intuitive predictions on the steady stress, and alternate, testable predictions on the ripple velocity. Although challenges remain, notably a failure to predict ripple rotation at grazing incidence angles, and a need to distinguish stress effects from those of redistributed atoms, this closer link to physical origins, and expanded predictive power for Argon-irradiated Silicon, make the model a potentially valuable stepping stone toward the goal of a predictive theory with the quantitative accuracy necessary for industrial relevance.

-
- [1] W. L. Chan and E. Chason. Making waves: kinetic processes controlling surface evolution during low energy ion sputtering. *J. Appl. Phys.*, 101:121301, 2007.
- [2] F. Frost, B. Ziberi, A. Schindler, and B. Rauschenbach. Surface engineering with ion beams: From self-organized nanostructures to ultra-smooth surfaces. *Appl. Phys. A*, 91:551–559, 2008.
- [3] S. Facsko, T. Dekorsy, C. Koerdt, C. Trappe, H. Kurz, A. Vogt, and H. L. Hartnagel. Formation of ordered nanoscale semiconductor dots by ion sputtering. *Science*, 285:1551–1553, 1999.
- [4] G. Ozaydin, A.S. Ozcan, Y.Y. Wang, K.F. Ludwig, H. Zhou, R.L. Headrick, and D.P. Siddons. Real-time x-ray studies of Mo-seeded Si nanodot formation during ion bombardment. *Applied Physics Letters*, 87:163104, 2005.
- [5] S. Macko, F. Frost, B. Ziberi, D.F. Forster, and T. Michely. Is keV ion-induced pattern formation on Si(001) caused by metal impurities? *Nanotechnology*, 21:085301, 2010.
- [6] R. Mark Bradley and Patrick D. Shipman. Spontaneous pattern formation induced by ion bombardment of binary compounds. *Physical Review Letters*, 105:145501, 2010.
- [7] R. Gago, L. Vásquez, O. Plantevin, T. H. Metzger, J. Muñoz-García, R. Cuerno, and M. Castro. Order enhancement and coarsening of self-organized silicon nanodot patterns induced by ion-beam sputtering. *Appl. Phys. Lett.*, 89:233101, 2006.
- [8] B. Ziberi, F. Frost, M. Tartz, H. Neumann, and B. Rauschenbach. Ripple rotation, pattern transitions, and long range ordered dots on silicon by ion beam erosion. *Appl. Phys. Lett.*, 92:063102, 2008.
- [9] C. S. Madi, B. P. Davidovitch, H. B. George, S. A. Norris, M. P. Brenner, and M. J. Aziz. Multiple bifurcation types and the linear dynamics of ion sputtered surfaces. *Phys. Rev. Lett.*, 101:246102, 2008.
- [10] S. Facsko, T. Bobek, A. Stahl, and H. Kurz. Dissipative continuum model for self-organized pattern formation during ion-beam erosion. *Phys. Rev. B*, 69:153412, 2004.
- [11] B. P. Davidovitch, M. J. Aziz, and M. P. Brenner. On the stabilization of ion sputtered surfaces. *Phys. Rev. B*, 76:205420, 2007.
- [12] R.M. Bradley. Redeposition of sputtered material is a nonlinear effect. *Physical Review B*, 83:075404, 2011.

- [13] S. A. Norris. Stability analysis of a viscoelastic model for ion-irradiated silicon. *Physical Review B*, 85:155325, 2012.
- [14] Charbel S. Madi and Michael J. Aziz. Multiple scattering causes the low energy-low angle constant wavelength bifurcation of argon ion bombarded silicon surfaces. *Applied Surface Science*, 258:4112–4115, 2012. (IINM2011 Bhubaneswar Conference Proceedings).
- [15] G. Ozaydin, Jr. K. F. Ludwig, H. Zhou, and R. L. Headrick. Effects of mo seeding on the formation of si nanodots during low-energy ion bombardment. *J. Vac. Sci. Technol. B*, 26:551, 2008.
- [16] G. Ozaydin-Ince and K. F. Ludwig Jr. In situ x-ray studies of native and mo-seeded surface nanostructuring during ion bombardment of si(100). *J. Phys. Cond. Matt.*, 21:224008, 2009.
- [17] Kun Zhang, Marc Brötzmann, and Hans Hofsäss. Surfactant-driven self-organized surface patterns by ion beam erosion. *New Journal of Physics*, 13:013033, 2011.
- [18] V. B. Shenoy, W. L. Chan, and E. Chason. Compositionally modulated ripples induced by sputtering of alloy surfaces. *Physical Review Letters*, 98:256101, 2007.
- [19] P. D. Shipman and R. M. Bradley. Theory of nanoscale pattern formation induced by normal-incidence ion bombardment of binary compounds. *Physical Review B*, 84:085420, 2011.
- [20] R. Mark Bradley. Theory of nanodot and sputter cone arrays produced by ion sputtering with concurrent deposition of impurities. *Physical Review B*, 83:195410, 2011.
- [21] R. M. Bradley. Surface instability of binary compounds caused by sputter yield amplification. *Journal of Applied Physics*, in press, 2012.
- [22] G. Abrasonis and K. Morawetz. Instability types at ion-assisted alloy deposition: from two-dimensional to three-dimensional nanopattern growth. *Physical Review B*, submitted, 2012. arXiv:1109.5461v2.
- [23] Scott A. Norris. A chemically-driven finite-wavelength instability in ion-irradiated compound semiconductors. arXiv:1205.6834v1 [cond-mat.mtrl-sci].
- [24] P. Sigmund. Theory of sputtering. I. Sputtering yield of amorphous and polycrystalline targets. *Phys. Rev.*, 184:383–416, 1969.
- [25] P. Sigmund. A mechanism of surface micro-roughening by ion bombardment. *J. Mater. Sci.*, 8:1545–1553, 1973.

- [26] R. M. Bradley and J. M.E. Harper. Theory of ripple topography induced by ion bombardment. *J. Vac. Sci. Technol.*, 6:2390–2395, 1988.
- [27] G. Carter and V. Vishnyakov. Roughening and ripple instabilities on ion-bombarded si. *Phys. Rev. B*, 54:17647–17653, 1996.
- [28] C. A. Volkert. Stress and plastic flow in silicon during amorphization by ion bombardment. *J. Appl. Phys.*, 70:3521, 1991.
- [29] C. C. Umbach, R. L. Headrick, and K.-C. Chang. Spontaneous nanoscale corrugation of ion-eroded SiO₂: The role of ion-irradiation-enhanced viscous flow. *Phys. Rev. Lett.*, 87:246104, 2001.
- [30] R. Cuerno, M. Castro, J. Muñoz-García, R. Gago, and L. Vásquez. Nanoscale pattern formation at surfaces under ion-beam sputtering: A perspective from continuum models. *Nuclear Instruments and Methods in Physics Research B*, 269:894–900, 2011.
- [31] Mario Castro and Rodolfo Cuerno. Hydrodynamic approach to surface pattern formation by ion beams. *Applied Surface Science*, 258:4171–4178, 2012.
- [32] M. Castro, R. Gago, L. Vásquez, J. Muñoz-García, and R. Cuerno. Solid flow drives surface nanopatterning by ion-beam irradiation. arXiv:1203.1167v1 [cond-mat.mtrl-sci].
- [33] Alexander Oron, Stephen H. Davis, and S. George Bankoff. Long-scale evolution of thin liquid films. *Reviews of Modern Physics*, 69:931–980, 1997.
- [34] H. Trinkaus and A. I. Ryazanov. Viscoelastic model for the plastic flow of amorphous solids under energetic ion bombardment. *Physical Review Letters*, 75:5072–5075, 1995.
- [35] H. Trinkaus. Dynamics of viscoelastic flow in ion tracks: origin of plastic deformation of amorphous materials. *Nuclear Instruments and Methods in Physics Research B*, 146:204–216, 1998.
- [36] E. Snoeks, T. Weber, A. Cacciato, and A. Polman. MeV ion irradiation-induced creation and relaxation of mechanical stress in silica. *J. Appl. Phys.*, 78:4723, 1995.
- [37] T. van Dillen, A. Polman, W. Fukarek, and A. van Blaaderen. Energy-dependent anisotropic deformation of colloidal silica particles under mev au irradiation. *Applied Physics Letters*, 78:910–912, 2001.
- [38] T. van Dillen, A. Polman, P. R. Onck, and E. van der Giessen. Anisotropic plastic deformation by viscous flow in ion tracks. *Physical Review B*, 71:024103, 2005.

- [39] K. Otani, X. Chen, J. W. Hutchinson, J. F. Chervinsky, and M. J. Aziz. Three-dimensional morphology evolution of SiO₂ patterned films under MeV ion irradiation. *J. Appl. Phys.*, 100:023535, 2006.
- [40] T. van Dillen, A. Polman, C. M. van Kats, and A. van Blaaderen. Ion beam-induced anisotropic plastic deformation at 300 keV. *Applied Physics Letters*, 83:4315–4317, 2003.
- [41] Y.-R. Kim, P. Chen, M. J. Aziz, D. Branton, and J. J. Vlassak. Focused ion beam induced deflections of freestanding thin films. *Journal of Applied Physics*, 100:104322, 2006.
- [42] H. B. George, Y. Tang, X. Chen, J. Li, J. W. Hutchinson, J. A. Golovchenko, and M. J. Aziz. Nanopore fabrication in amorphous Si: Viscous flow model and comparison to experiment. *Journal of Applied Physics*, 108:014310, 2010.
- [43] S. A. Norris, J. Samela, L. Bukonte, M. Backman, D. F. K. Nordlund, C.S. Madi, M.P. Brenner, and M.J. Aziz. Molecular dynamics of single-particle impacts predicts phase diagrams for large scale pattern formation. *Nature Communications*, 2:276, 2011.
- [44] Lawrence E. Malvern. *Introduction to the Mechanics of a Continuous Medium*. Prentice Hall, 1977. ISBN: 0134876032.
- [45] M. Moseler, P. Gumbsch, C. Casiraghi, A. C. Ferrari, and J. Robertson. The ultrasmoothness of diamond-like carbon surfaces. *Science*, 309:1545–1548, 2005.
- [46] N. Kalyanasundaram, M. Ghazisaeidi, J. B. Freund, and H. T. Johnson. Single impact crater functions for ion bombardment of silicon. *Appl. Phys. Lett.*, 92:131909, 2008.
- [47] N. Kalyanasundaram, M. C. Moore, J. B. Freund, and H. T. Johnson. Stress evolution due to medium-energy ion bombardment of silicon. *Acta Materialia*, 54:483–491, 2006.
- [48] C. S. Madi. *Linear Stability and Instability Patterns in Ion Bombarded Silicon Surfaces*. PhD thesis, Harvard University, 2011.
- [49] C. S. Madi and M. Aziz. private communication.
- [50] S. E. Orchard. On surface levelling in viscous liquids and gels. *Appl. Sci. Res.*, 11A:451, 1962.
- [51] C. S. Madi, H. B. George, and M. J. Aziz. Linear stability and instability patterns in ion-sputtered silicon. *J. Phys. Cond. Matt.*, 21:224010, 2009.
- [52] S. Vauth and S. G. Mayr. Relevance of surface viscous flow, surface diffusion, and ballistic effects in keV ion smoothing of amorphous surfaces. *Phys. Rev. B*, 75:224107, 2007.

- [53] D. J. Eaglesham, A. E. White, L. C. Feldman, N. Moriya, and D. C. Jacobson. Equilibrium shape of Si. *Phys. Rev. Lett.*, 70:1643, 1993.
- [54] P. F. A. Alkemade. Propulsion of ripples on glass by ion bombardment. *Phys. Rev. Lett.*, 96:107602, 2006.
- [55] Hubert Gnaser, Bernhard Reuscher, and Anna Zeuner. Propagation of nanoscale ripples on ion-irradiated surfaces. *Nuclear Instruments and Methods in Physics Research B*, 285:142–147, 2012.
- [56] Nagarajan Kalyanasundaram, Molly Wood, Jonathan B. Freund, and H.T. Johnson. Stress evolution to steady state in ion bombardment of silicon. *Mechanics Research Communications*, 35:50–56, 2008.
- [57] C. S. Madi, E. Anzenberg, K. F. Ludwig Jr., , and M. J. Aziz. Mass redistribution causes the structural richness of ion-irradiated surfaces. *Phys. Rev. Lett.*, 106:066101, 2011.
- [58] M. Z. Hossain, K. Das, J. B. Freund, and H. T. Johnson. Ion impact crater asymmetry determines surface ripple orientation. *Applied Physics Letters*, 99:151913, 2011.
- [59] N. Kalyanasundaram, J. B. Freund, and H. T. Johnson. Atomistic determination of continuum mechanical properties of ion-bombarded silicon. *Journal of Engineering Materials and Technology*, 127:457–461, 2005.

Appendix A: Solution of the Linearized Equations

In this Appendix we present the details of the calculation by which the dispersion relation (20) was obtained.

General solution from the bulk Equations. In the linear ansatz (19), the (already-linear) Stokes equations become

$$-ik_1 p(z) + \eta [-(k_1^2 + k_2^2)u + u''] = 0 \quad (\text{A1})$$

$$-ik_2 p(z) + \eta [-(k_1^2 + k_2^2)v + v''] = 0 \quad (\text{A2})$$

$$-p'(z) + \eta [-(k_1^2 + k_2^2)w + w''] = 0 \quad (\text{A3})$$

$$ik_1 u + ik_2 v + w' = 0 \quad (\text{A4})$$

The first step in the solution is to eliminate u, v, w in the following manner:

1. differentiate Eqn.(A4), to get an expression for w''
2. insert the resulting expression for w'' into Eqn.(A3)
3. differentiate the result to get an expression for $p''(z)$
4. in the resulting expression, eliminate w' using (A4)
5. finally, eliminate u and v using (A1) and (A2)

The resulting homogeneous equation for $p(z)$ is

$$p'' - (k_1^2 + k_2^2)p = 0$$

with solutions

$$p(z) = \bar{A} \cosh(Rz) + \bar{B} \sinh(Rz), \quad (\text{A5})$$

where $R = \sqrt{k_1^2 + k_2^2}$.

From here, we simply insert the solution (A5) back into (A1)-(A3) to get inhomogeneous equations for u, v, w : these have solutions

$$u = C \cosh(Rz) + D \sinh(Rz) + \frac{ik_1}{2\eta R} z [\bar{B} \cosh(Rz) + \bar{A} \sinh(Rz)] \quad (\text{A6})$$

$$v = E \cosh(Rz) + F \sinh(Rz) + \frac{ik_2}{2\eta R} z [\bar{B} \cosh(Rz) + \bar{A} \sinh(Rz)] \quad (\text{A7})$$

$$w = G \cosh(Rz) + H \sinh(Rz) + \frac{1}{2\eta} z [\bar{A} \cosh(Rz) + \bar{B} \sinh(Rz)]. \quad (\text{A8})$$

At this point, however, we have too many constants because we first differentiated Eqn.(A4), raising its order. Re-considering Eqn.(A4) in its original form, we insert (A6)-(A8) and collect like terms in $\sinh(Rz)$ and $\cosh(Rz)$ to obtain

$$\begin{aligned}\frac{ik_1}{R}D + \frac{ik_2}{R}F + \frac{1}{2\eta R}\bar{B} + G &= 0 \\ \frac{ik_1}{R}C + -\frac{ik_2}{R}E + \frac{1}{2\eta R}\bar{A} + H &= 0.\end{aligned}$$

From here, we choose to replace \bar{A} and \bar{B} with the other constants to obtain the following expressions for the pressure and velocity:

$$\begin{aligned}p_1(z) &= -2\eta [(RH + ik_1C + ik_2E) \cosh(Rz) + (RG + ik_1D + ik_2F) \sinh(Rz)] \\ u_1(z) &= C \cosh(Rz) + D \sinh(Rz) - \frac{ik_1}{R} \left[\begin{array}{l} (RG + ik_1D + ik_2F) z \cosh(Rz) \\ + (RH + ik_1C + ik_2E) z \sinh(Rz) \end{array} \right] \\ v_1(z) &= E \cosh(Rz) + F \sinh(Rz) - \frac{ik_2}{R} \left[\begin{array}{l} (RG + ik_1D + ik_2F) z \cosh(Rz) \\ + (RH + ik_1C + ik_2E) z \sinh(Rz) \end{array} \right], \quad (\text{A9}) \\ w_1(z) &= G \cosh(Rz) + H \sinh(Rz) - \left[\begin{array}{l} (RG + ik_1D + ik_2F) z \sinh(Rz) \\ + (RH + ik_1C + ik_2E) z \cosh(Rz) \end{array} \right]\end{aligned}$$

where $R = \sqrt{k_1^2 + k_2^2}$, and C, D, E, F, G, H are integration constants.

Integration constants from Boundary Conditions. To find the integration constants, we apply the linearized versions of the three no penetration/slip conditions (11) at the amorphous/crystalline interface $z = h_1(x, y)$, and the three stress balance conditions (12) at the free interface $z = h_0 + h_1(x, y)$. At the bottom of the film, $z = g_1(x, y) = h_1(x, y)$, the no-slip boundary condition (11) linearizes to the related condition

$$\mathbf{v}_1(x, y, 0) + \frac{\partial \mathbf{v}_0}{\partial z}(x, y, 0) \cdot h_1 = 0 \quad (\text{A10})$$

at $z = 0$, giving

$$\begin{aligned}C &= -3fA \sin(2\theta) h_1(x, y) \\ E &= 0 \\ G &= 0\end{aligned} \quad (\text{A11})$$

At the top of the film, $z = h_0 + h_1(x, y)$, we apply the stress condition (12); again, this linearizes to a related condition

$$\mathbf{T}_0 \cdot \hat{\mathbf{n}}_1 + \mathbf{T}_1 \cdot \hat{\mathbf{n}}_0 = -\gamma \kappa_1 \hat{\mathbf{n}}_0$$

at $z = h_0$, which forms a matrix equation for the remaining constants $\{D, F, H\}$:

$$\begin{bmatrix} R\bar{C} + \frac{k_1^2}{R} (\bar{C} + 2Q\bar{S}) & \frac{k_1 k_2}{R} (\bar{C} + 2Q\bar{S}) & -2ik_1 Q\bar{C} \\ \frac{k_1 k_2}{R} (\bar{C} + 2Q\bar{S}) & R\bar{C} + \frac{k_2^2}{R} (\bar{C} + 2Q\bar{S}) & -2ik_2 Q\bar{C} \\ -2ik_1 Q\bar{C} & -2ik_2 Q\bar{C} & 2R(\bar{C} - Q\bar{S}) \end{bmatrix} \begin{bmatrix} D \\ F \\ H \end{bmatrix} = \begin{bmatrix} \bar{\alpha} \\ \bar{\beta} \\ \bar{\gamma} \end{bmatrix}, \quad (\text{A12})$$

where $Q = h_0 R$, $\bar{C} = \cosh(Q)$, $\bar{S} = \sinh(Q)$, and

$$\begin{bmatrix} \bar{\alpha} \\ \bar{\beta} \\ \bar{\gamma} \end{bmatrix} = -\gamma \begin{bmatrix} 0 \\ 0 \\ R^2 \end{bmatrix} + 6\eta f A h_1 \begin{bmatrix} ik_1 \cos(2\theta) \\ ik_2 \cos^2(\theta) \\ 0 \end{bmatrix} + 3\eta f A h_1 \sin(2\theta) \begin{bmatrix} R\bar{S} + \frac{k_1^2}{R} (\bar{S} + 2Q\bar{C}) \\ \frac{k_1 k_2}{R} (\bar{S} + 2Q\bar{C}) \\ -2ik_1 Q \sinh(Q) \end{bmatrix}. \quad (\text{A13})$$

The three column vectors on the right hand side of Eqn.(A13) represent, respectively, the effects of surface tension, the beam stress acting in the bulk, and the effect under that stress of the non-planar bottom boundary.

The solution to Eqn.(A12) can be found using Cramer's Rule or a computer algebra system, yielding the result

$$\begin{aligned} D &= \frac{1}{\Delta} [2\bar{\alpha} R^2 (\bar{C}^2 - Q\bar{S}\bar{C}) + 2k_2 (\bar{\alpha} k_2 - \bar{\beta} k_1) (\bar{C}^2 + Q\bar{S}\bar{C} + 2Q^2) + 2i\bar{\gamma} k_1 R Q \bar{C}^2] \\ F &= \frac{1}{\Delta} [2\bar{\beta} R^2 (\bar{C}^2 - Q\bar{S}\bar{C}) - 2k_1 (\bar{\alpha} k_2 - \bar{\beta} k_1) (\bar{C}^2 + Q\bar{S}\bar{C} + 2Q^2) + 2i\bar{\gamma} k_2 R Q \bar{C}^2], \quad (\text{A14}) \\ H &= \frac{1}{\Delta} [2iR (\bar{\alpha} k_1 + \bar{\beta} k_2) Q \bar{C}^2 + 2\bar{\gamma} R^2 (\bar{C}^2 + Q\bar{S}\bar{C})] \end{aligned}$$

where $\bar{\alpha}$, $\bar{\beta}$, $\bar{\gamma}$ remain as given in Eqn.(A13) and

$$\Delta = 2R^3 \cosh(Q) [1 + 2Q^2 + \cosh(2Q)]$$

is the determinant of the matrix on the left hand side of Eqn.(A12).

Dispersion Relation from the Kinematic Condition. Having uniquely determined the pressure and velocity fields, it remains to apply the kinematic condition (13), which linearizes to

$$\sigma(k_1, k_2) = w_1(h_0) - u_0(h_0) \frac{\partial h_1}{\partial x} - v_0(h_0) \frac{\partial h_1}{\partial y}. \quad (\text{A15})$$

From the general solution (A9) in the main text, and the solutions (A11) and (A14) for the integration constants, we can evaluate $w_1(h_0)$, which leads directly to the dispersion relation (20) in the main text.